Methodology and Validation of UAV-Based Video Analysis Approach for Tracking Earthquake-Induced Building Displacements

X. Wang[1]; C. E. Wittich, A.M.ASCE[2]; T. C. Hutchinson, M.ASCE[3]; Yehuda Bock[4]; Dara Goldberg[5]; Eric Lo[6]; and F. Kuester[7]

Abstract: Unmanned aerial vehicle (UAV) imagery has recently emerged as a promising alternative for operational condition inspection and postdisaster damage assessment of civil structures (e.g., bridges and buildings). However, the use of such sensing techniques for quantitatively tracking the subtle (centimeter-level) variations of the responses of structures has been limited. This is largely due to the difficulties related to obtaining accurate location measurements of the cameras aboard small UAV platforms. To address this research gap, we propose a video analysis methodology for tracking the displacement response of buildings subject to dynamic loads using camera-equipped UAV platforms. The movement of the image sensor on-board the UAV platform is corrected to allow image-by-image natural feature detection and tracking. In this methodology, the image processing procedure does not rely on the camera position and orientation. As such, the approach first corrects for image distortion introduced by UAV drift and subsequently extracts the dynamic displacements of the building by tracking its natural features at the pixel level. Motion-tracking errors are investigated by analyzing the building displacements using pre- and postevent videos. The proposed methodology is validated by monitoring the dynamic response of a full-scale building during a shake table test program. Uniquely, global positioning system (GPS) displacement measurements are independently utilized to validate the proposed UAV video-based method and assess its effectiveness for capturing the dynamic responses of full-scale structures with a level of precision that is sufficient for engineering applications (less than 2 cm root-mean-square errors). **DOI: 10.1061/(ASCE)CP.1943-5487.0000928.**

Author keywords: Feature detection; Motion tracking; Photogrammetry; Shake table tests; Unmanned aerial vehicles; Vision-based sensing.

Introduction

Vision-based monitoring systems have attracted significant research attention among civil engineers for the past few decades as a cost-effective and nonintrusive sensing technique. Imagery data collected using such sensing systems have been applied to detect structural surface damage and defects (e.g., Abdel-Qader et al. 2003; Hutchinson and Chen 2006; Koch et al. 2012; Torok et al. 2013; Yeum and Dyke 2015; Gao and Mosalam 2018) and to track structural responses under dynamic loading environments (e.g., Wahbeh et al. 2003; Hutchinson and Kuester 2004; Lee and Shinozuka 2006; Fukuda et al. 2010; Yoon et al. 2016). The recent availability of commercial unmanned aerial vehicle (UAV) platforms with on-board cameras offers even more flexibility and mobility for image data collection. These camera-equipped airborne platforms are particularly useful when access to camera views is difficult or even impossible for ground-based image sensors (e.g., building roofs or the underside of bridge decks). Recent applications of UAV imagery involve operational condition inspection of civil structures (e.g., Morgenthal and Hallermann 2014; Ellenberg et al. 2016; Yoon et al. 2017; Reagan et al. 2018) as well as postdisaster assessment of structural damage and geohazards (e.g., Meyer et al. 2015; Franke et al. 2016; Dominici et al. 2017; Wood et al. 2017).

Despite the extensive research efforts on UAV vision-based monitoring of civil structures, the application of such sensing techniques for quantitatively tracking the subtle (centimeter-level) variations of dynamic structural responses has been limited. Unlike ground-based cameras that remain essentially stationary, UAV-mounted cameras are subjected to the ego-motion (colloquially referred to as drift) of the UAVs during flight operations. Although advanced positioning techniques (e.g., real-time kinematic and postprocessing kinematic) may provide high-precision (centimeter-level) flight position data, these techniques are not implemented by the majority of small commercial UAV platforms. As a result, a lack of precise position information for the UAVs and the movement of the on-board cameras during navigation and hold, which are often mounted on gimbals, pose major challenges to obtaining accurate structural responses from aerial imagery. In a recent study,

[1]Postdoctoral Researcher, Dept. of Structural Engineering, Univ. of California, San Diego, La Jolla, CA 92093-0085.

[2]Assistant Professor, Dept. of Civil Engineering, Univ. of Nebraska-Lincoln, Lincoln, NE 68583-0855. ORCID: https://orcid.org/0000-0002-2678-7310

[3]Professor, Dept. of Structural Engineering, Univ. of California, San Diego, La Jolla, CA 92093-0085 (corresponding author). ORCID: https://orcid.org/0000-0001-9109-7896. Email: tara@ucsd.edu; tahutchinson@eng.ucsd.edu

[4]Distinguished Researcher, Scripps Institution of Oceanography, Univ. of California, San Diego, La Jolla, CA 92093-0085.

[5]Postdoctoral Researcher, Scripps Institution of Oceanography, Univ. of California, San Diego, La Jolla, CA 92093-0085.

[6]Research and Development Engineer, Qualcomm Institute, Univ. of California, San Diego, La Jolla, CA 92093-0085.

[7]Professor, Dept. of Structural Engineering, Univ. of California, San Diego, La Jolla, CA 92093-0085.

Note. This manuscript was submitted on April 26, 2019; approved on June 9, 2020; published online on August 27, 2020. Discussion period open until January 27, 2021; separate discussions must be submitted for individual papers. This paper is part of the ***Journal of Computing in Civil Engineering***, © ASCE, ISSN 0887-3801.

Yoon et al. (2018) proposed a UAV-based structural displacement monitoring method and validated their results using small-scale prototype structure experiments. In their method, the on-board camera motion was resolved with the placement of background reference objects (in this case checkerboards). However, the conditions used for recovering the camera motion (e.g., controlled indoor laboratory environment, close camera-to-scene distance, and the presence of reference objects) may not be feasible for structural monitoring applications in the field. Therefore, there is a strong need to develop methodologies for UAV-based motion tracking specific to capturing dynamic structural responses without the need to recover the camera (or UAV) motion information and to evaluate the benefits and limitations of such motion-tracking methodologies.

To this end, a UAV-based video analysis methodology is proposed. Its reliability is assessed using data collected from a full-scale building tested in a controlled setting atop an outdoor shake table. The test building was subjected to a sequence of earthquake input motions using the Large High Performance Outdoor Shake Table (LHPOST) experimental facility at the University of California, San Diego (UCSD) (Wang et al. 2016, 2018). During the simulated earthquake tests, the building responses were monitored using conventional attached analog sensors, including accelerometers and displacement transducers as well as global positioning systems (GPS) at the roof level. In addition, point cloud data of the test site and the test building was collected using a light and ranging detection (LiDAR) scanner prior to the test phase in an effort to provide reliable and accurate geometric information of the test site and the test building in its baseline condition.

Facilitated by an outdoor test environment, multiple UAVs were employed to record aerial and elevation-view videos of the building during these earthquake tests. While this platform has a built-in gimbal to stabilize video recordings, three primary issues preclude accurate displacement measurement from individual video frames: (1) image distortion due to the camera lens (e.g., straight lines appear curved due to the lens curvature), (2) UAV drift-induced image misalignment with respect to the ground over the duration of an individual earthquake test, and (3) nonorthogonal camera orientation that introduces perspective distortion to individual video frames (e.g., parallel lines appear to converge). Analog sensor and GPS measurements from these tests provide a unique dataset for comparison with UAV-collected video to assess the proposed tracking methodology.

In the proposed UAV-based video analysis methodology, the image distortion caused by the camera lens and drift of the UAVs is first corrected on a frame-by-frame basis; subsequently, the undistorted images are used for motion tracking of the building using natural features at the pixel level. The methodology is evaluated by investigating the characteristics of motion-tracking errors. Motion-tracking errors are assessed by analyzing the building displacements extracted from pre- or postevent videos in an effort to further correct the video analysis results during the earthquake shaking. Comparison of the video-based results with GPS measurements demonstrates the effectiveness of the proposed UAV-based methodology for successfully quantifying the dynamic responses of full-scale buildings. Uniquely, without relying on the position of UAV on-board cameras, the video analysis results achieve a high level of precision (<2 cm), which is considered acceptable for many structural engineering applications.

Full-Scale Building Shake Table Test Program Used for Methodology Validation

Successful implementation of the proposed video analysis methodology is based on UAV videos and other datasets (e.g., GPS measurements, LiDAR point cloud) collected during a full-scale building shake table test program. As such, this section provides first an overview of the test building and its test protocol. In addition, the UAV video monitoring plan utilized during the earthquake tests and the auxiliary datasets used for video analysis are described. Information presented in this section facilitates the understanding of the proposed UAV-based video analysis methodology discussed later.

Overview of Test Program

Constructed with a structural system entirely using cold-formed steel (CFS), the six-story test building was designed to emulate a midrise residential dwelling with structural shear walls and floor diaphragms framed of CFS members (e.g., studs and joists) and sheathed by steel sheet material. The exterior of the building was clad in fire-resistant gypsum board with window openings as might be utilized in conventional multifamily architecture. The building was assumed to be located in a high seismic region near downtown Los Angeles, with its design basis complying with current code provisions (AISI 2007, 2012; ASCE 2010). As shown in Fig. 1, the test building had a uniform plan dimension of 10.4×7.3 m, occupying almost the entire 12.2×7.6-m shake table footprint. The floor-to-floor height of the building was 3.05 m for all six stories, resulting in a total height of 18.3 m of the roof above the ground level. The total weight of the building was ~1,160 kN, resulting in a fundamental period of approximately 0.3 s in the longitudinal (shaking) direction under its initial (undamaged) condition (Wang and Hutchinson 2020). Additional details regarding the building design and expected seismic performance may be found in Wang et al. (2016, 2018).

The test protocol imposed on this building consisted of a sequence of earthquake and live fire tests in three sequential phases. During the first (prefire) earthquake test phase, the building was subjected to seven earthquake motions of increasing intensity: serviceability, design, and maximum considered earthquake (MCE) target scaled (refer to Table 1 for details). Subsequently, a total of six live fire tests were conducted on the earthquake-damaged building at Levels 2 and 6. The test program concluded with two postfire earthquake tests (serviceability followed by MCE). It is noted that all earthquake input motions were applied in the east-west direction using the single-axis shake table coinciding with the longitudinal axis of the building (Fig. 1). Consequently, the building displacement responses in the transverse direction (short axis of the building) were significantly smaller than their counterparts in the longitudinal (shaking) direction.

UAV Video Monitoring Plan and Auxiliary Datasets for Video Analysis

During the shake table tests, two small UAVs (Phantom 3 Pro, DJI, Los Angeles) were employed to video-record the building dynamic displacement responses during a sequential series of seven earthquake tests at different motion intensities (EQ4–EQ9, see Table 1). The test videos were all recorded using the on-board cameras with a rate of 30 frames per second and a resolution of $3,840 \times 1,920$ pixels. Two strategic viewpoints were consistently employed for the video recordings, namely, top views monitoring the building roof and the ground level [Fig. 2(a)], as well as elevation views monitoring the building facades. Importantly, these UAV platforms are mounted with very low-resolution positioning sensors suitable only for navigation; therefore, the accurate location and orientation of the vehicles and the on-board cameras during the video recording is best estimated using photogrammetric techniques, such as the Perspective-n-Point (PnP) method (e.g., Gao et al. 2003; Lepetit et al. 2009) or the structure-from-motion (SfM) method

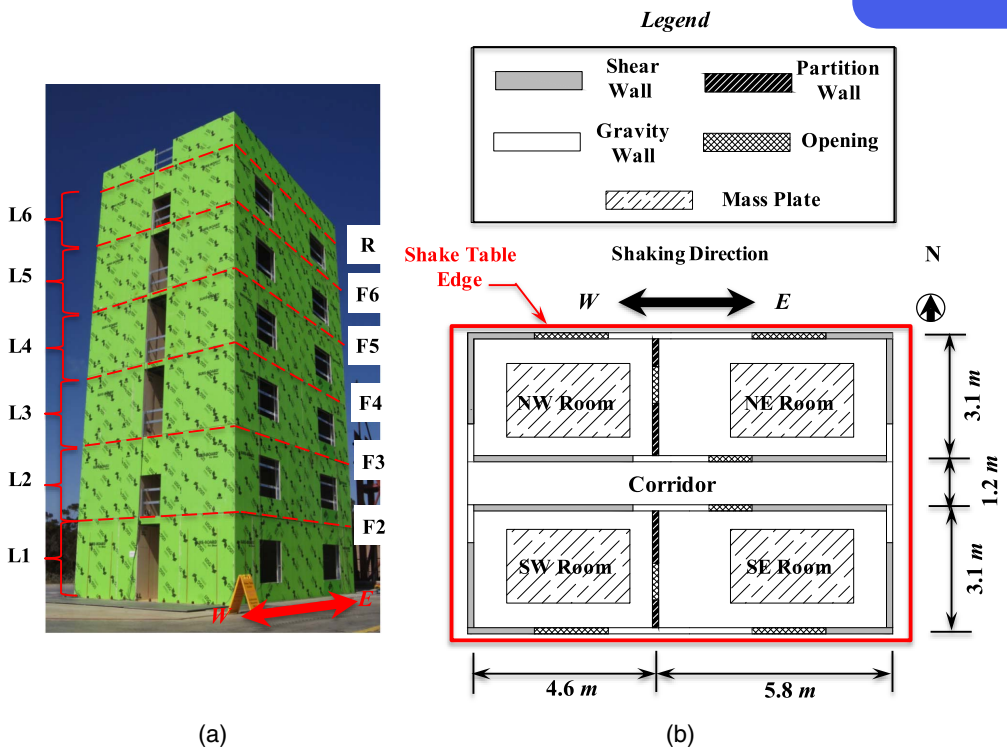

Fig. 1. Test building: (a) isometric view (arrows denote earthquake shaking direction); and (b) building plan layout (typical of floors 2–6; hatched boxed areas denote mass plates).

Table 1. Summary of the peak and residual roof displacements associated with individual earthquake tests and the corresponding camera views of the UAV test videos

Earthquake test date	Test name	Performance level[a]	Roof longitudinal displacement		Camera view[d]
			Peak[b] (cm)	Residual[c] (cm)	
Day 1(June 13, 2016)	EQ1:RIO-25	SLE (25% design)	2.5	0.0	No videos recorded
	EQ2:CNP-25		4.8	0.0	
	EQ3:CUR-25		3.3	0.0	
Day 2 (June 15, 2016)	EQ4:CNP-25		5.2	0.0	North, south
	EQ5:CNP-50	50% design	10.0	0.0	North, **top**
	EQ6:CNP-100	Design	21.2	0.0	North
Day 3 (June 17, 2016)	EQ7:CNP-150	MCE (150% design)	41.3	1.4 (0.1%)	North, **top**
		Fire test sequence (June 27–29, 2016)			
Day 4 (July 1, 2016)	EQ8:RIO-25	SLE	2.8	0.0	North, top
	EQ9:RRS-150	MCE	79.5	22.0 (1.2%)	Isometric, **top**

[a]SLE = service level earthquake; and MCE = maximum considered earthquake.
[b]Residual displacement represents the averaged displacement (5-s window) at the completion of the earthquake shaking, percentage value in the parentheses represents the roof drift ratio (normalized by building height).
[c]Peak displacement represents the absolute maximum displacement during the earthquake shaking.
[d]North and south refer to an elevation view of either the north or south building facade; Top refers to a looking-down plan view of the building roof and the ground; Isometric refers to an oblique elevation view isometrically looking at the northwest corner of the building. Note that bold **Top** refers to test videos used in the validation studies herein.

(e.g., Westoby et al. 2012; Schonberger and Frahm 2016). These methods estimate the relative location and orientation of a camera (referred to as camera pose) using corresponding points in the world coordinates and their projections in the pixel coordinates. However, the camera pose recovered using these techniques may involve large uncertainties due to the following two practical limitations: (1) insufficient ground-level feature points (<5 points) with precisely known positions in the world coordinates, and (2) large distances between the camera and ground level (40–60 m) during the video recording. These physical constraints create challenges for maintaining high levels of accuracy and robustness with regard to the use of the estimated camera pose to precisely reproject the image features in the video analysis. In this regard, our motivation is to develop a video analysis methodology that overcomes these limitations and maintains an accuracy level sufficient for structural dynamic response monitoring.

To validate the UAV-based motion-tracking results, three geodetic-quality Topcon NET G3-A GPS stations were installed on the roof of the building [Figs. 2(a and c)]. Displacements during

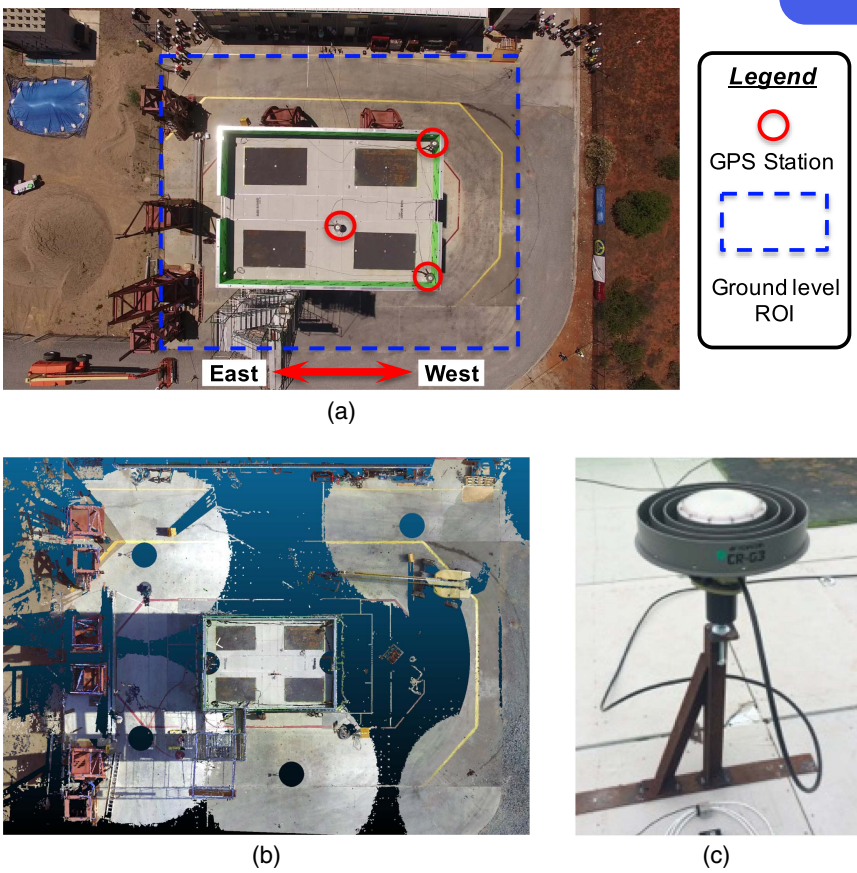

Fig. 2. (a) Sample UAV top-view image frame (taken during Test EQ7, double-side arrow denotes the direction of shaking); (b) orthoimage generated using LiDAR point cloud data; and (c) roof GPS antenna and its support (center station).

the earthquake tests were recorded using these stations at a high rate (10 Hz) with respect to a fourth station installed at a fixed reference station at ground level off of the shake table platen (~50 m to the west). In the context of the present application, the GPS sampling rate of 10 Hz is considered to be sufficient for validation because (1) the natural frequency of the fundamental mode of the building was <4 Hz under its initial condition and decreased gradually as a result of accumulated structural damage during the test sequence, and (2) the midrise test building response was dominated by its fundamental mode during the earthquake tests (Wang and Hutchinson 2020). The coordinates of the reference station were estimated in a global reference frame maintained by the International *Global* Navigation Satellite Systems Service prior to the building experiments. The positions of the roof stations were estimated in north, east, and vertical directions in the same reference frame with an accuracy of several millimeters. It is noted that the longitudinal (shaking) direction of the building coincides with the east-west direction of the GPS global reference frame. In this study, the roof displacements measured by the center GPS station were used for results validation due to the following two considerations: (1) the center station was located at the approximate geometric center of the roof footprint, and (2) the roof displacements measured at three different locations varied only slightly (<0.5 cm). In addition, high-resolution point cloud data of the test site and building were collected prior to the test phase using a terrestrial LiDAR scanner (Focus3D S120, FARO Technologies, Lake Mary, Florida). These point cloud data provided reliable and high-accuracy (subcentimeter-level precision) geometry measurements of the test site and the building in its baseline condition [Fig. 2(b)].

Table 1 summarizes the peak and residual roof longitudinal displacements of the test building measured by GPS (center station) and the camera views of the test videos associated with individual earthquake tests. To validate the proposed methodology, the dynamic roof displacements as measured via GPS are compared with the displacements calculated using the top-view test videos recorded during three earthquake tests: EQ5 (50% design event), EQ7 (MCE event or 150% design event), and EQ9 (MCE level or 150% design event). The top-view video taken during test EQ8 is not analyzed in this study due to the very low amplitude of the roof displacements (<3 cm in the direction of shaking). The residual roof displacement remained small during all earthquake tests (including EQ5 and EQ7) except the final test (EQ9). The building underwent excessively large roof residual drift demands (~22 cm, or a drift ratio of ~1.2%) following the final earthquake test (EQ9), resulting in a soft-story mechanism at Level 2 and a near-collapse condition of the test building at the end of the test program (Hutchinson et al. 2018).

Problem Statement and Proposed Methodology

The objective of UAV-based motion-tracking methodology as proposed herein is to extract with reasonable accuracy the dynamic roof displacements of buildings using top-down-view videos taken during earthquake shaking. Two assumptions are adopted to simplify the motion-tracking problem: (1) the in-plane movement of the roof is rigid (i.e., no differential displacements between different locations on the roof), and (2) vertical displacements

are negligible (i.e., no overturning rotation). These assumptions are justified in the dataset used for validation by assessing the GPS measurements, where it is noted that both the vertical roof displacements and the differential displacements in the horizontal directions measured at the different locations remained sufficiently small (<0.5 cm). Consequently, the problem reduces to an in-plane tracking problem with three unknowns of the roof motion: the displacements in the two translational directions and one in-plane rotation. In addition, the LiDAR data confirm that the elevation of the ground-level background region [regions padded with concrete, see Fig. 2(a)] varies only slightly across the large footprint at the ground surface (<10 cm). Because the elevation variation of the ground level was much smaller than the camera-to-ground distance (30–60 m from the camera to the ground level) during all video recordings, this region is considered as a two-dimensional planar region in the video analysis. Because no artificial targets were used during the tests to support the UAV-based video monitoring, the proposed motion-tracking algorithm relies entirely on the natural image features of the ground level and the building roof. Such a condition would emulate field practice as well, thus this scenario represents a realistic challenge when applying the proposed methodology outside of a controlled laboratory setting.

Proposed Methodology

Fig. 3 provides a flowchart of the proposed UAV-based video analysis methodology for tracking the dynamic displacements of the building during the earthquake shaking. The first and second steps aim to address the two primary sources of image distortion related to the recorded UAV videos, namely: (1) lens distortion, and (2) UAV drift-induced frame misalignment and perspective distortion. Following these steps, the recorded video frames represent a sequence of orthorectified images stabilized at the ground level. The stabilized image sequence allows for detecting pixel-based building features, namely, the roof in this validation case, and subsequently extracting the roof displacements by analyzing the frame-to-frame correspondences of the identified image features. For this exercise, the motion-tracking procedures are implemented in MATLAB (version 2017b) using built-in functions in the Computer Vision Toolbox. Details related to each of the three analysis steps are discussed in the following sections.

The three-step motion-tracking procedures produce a sequence of image frames stabilized at the ground level. However, they may not be sufficient to completely correct for UAV drift-induced distortion at the roof level. Although the stationary ground level during earthquake shaking allows frame-by-frame alignment via matching of the ground-level features, this same strategy is not applicable for correcting the drift-induced misalignment at the roof level, because the roof footprint was displaced during the earthquake tests. In addition, insufficient accuracy for the location and orientation of the on-board camera estimated using vision-based methods precludes the use of image reprojection to correct for UAV drift-induced distortion at the roof level.

To address this challenge, an alternative method is proposed, namely, by investigating the displacements extracted from the pre- or postevent videos (20–30 s before or after an earthquake test). Because the test building was stationary during the pre- and postevent stages, the roof displacements were considered negligibly small. In addition, the UAV was operated in hover mode during the video recording, and therefore it is reasonable to assume

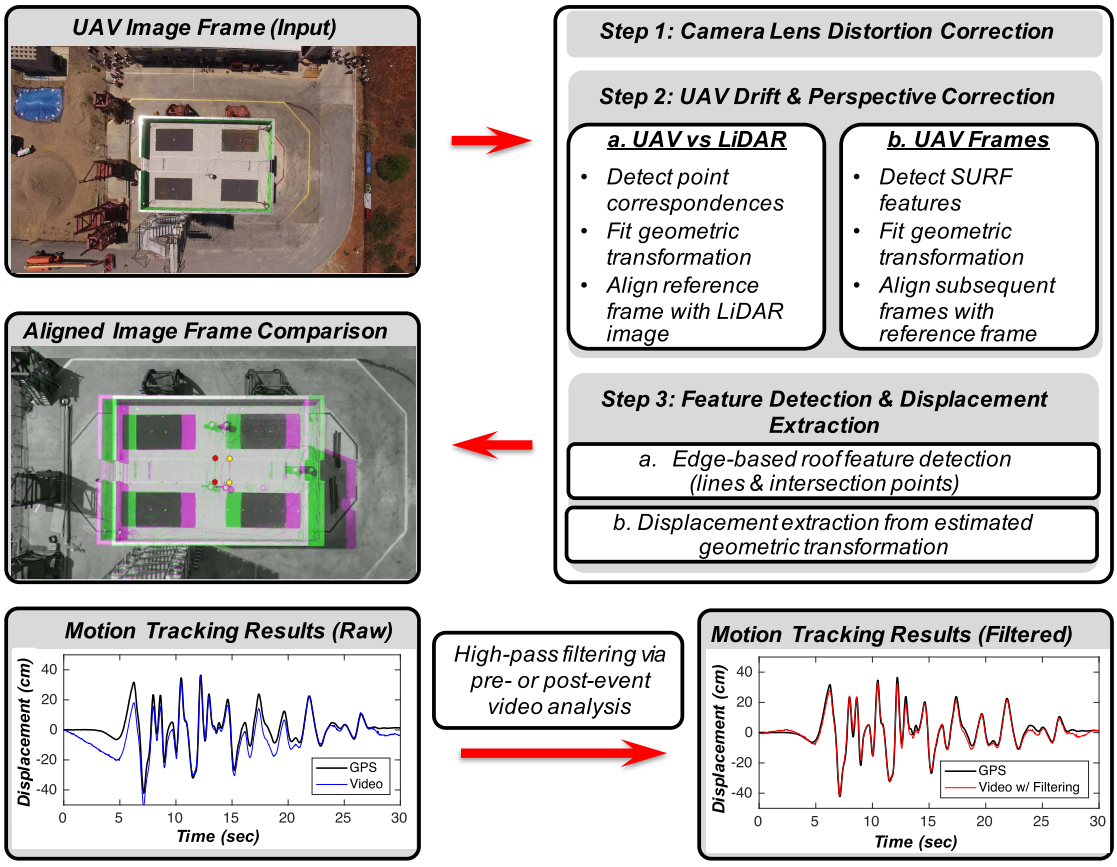

Fig. 3. Flowchart depicting the proposed UAV-based video analysis methodology.

J. Comput. Civ. Eng., 2020, 34(6): 04020045

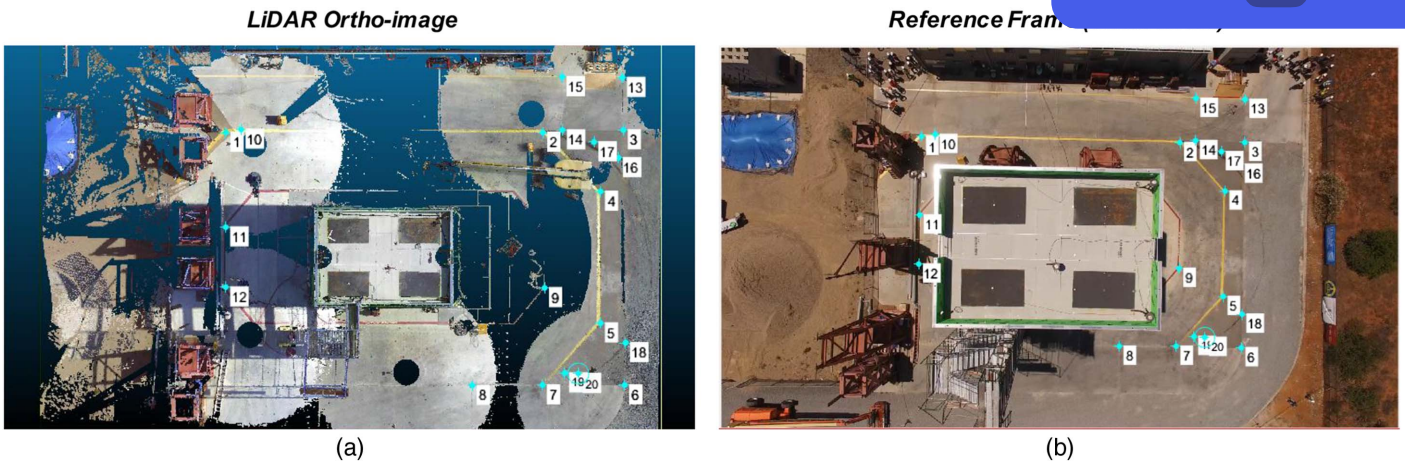

Fig. 4. Matched ground-level feature points between (a) LiDAR orthoimage; and (b) video reference frame.

that the effect of UAV drift-induced distortion on the video analysis results during the pre- or postevent are consistent with those during the earthquake. Consequently, the pre- or postevent video analysis results provide guidance on the selection of a high-pass corner frequency for correcting the effect of UAV drift-induced distortion at the roof level. The filtering strategy determined using the pre- or postevent video analysis is then applied to obtain the final roof dynamic displacements during the earthquake shaking. In what follows, each of the aforementioned steps is discussed in greater detail.

Camera Lens Distortion Correction

Step 1 of the proposed methodology aims to remove the effects of lens distortion, particularly in the form of barrel distortion in which straight lines appear as if they are curved around a barrel. In this step, each video frame is undistorted, yielding a rectilinear projection using lens distortion parameters estimated through a checkerboard calibration procedure applied to the UAV on-board cameras. The calibration procedures utilized to determine the lens distortion parameters are well documented in Bouguet (2015), and therefore details regarding the implementation of lens distortion correction are not discussed herein.

UAV Drift and Perspective Correction

The purpose of Step 2 is to stabilize the recorded UAV video frames at the ground level by correcting the perspective distortion introduced by the UAV's drift and the frame-to-frame misalignment. To facilitate the discussion on the analysis procedures, the first video frame is defined herein as the *reference frame*, whereas all remaining video frames are defined as the *subsequent frames*. The reference frame was selected to represent the test building in a stationary condition (a few seconds before the onset of an earthquake test). The drift-induced perspective distortion and frame-to-frame misalignment are corrected via the following two sequential substeps: (1) orthorectifying the reference video frame using the LiDAR orthoimage, and (2) aligning all subsequent frames to the orthorectified reference frame. Because no artificial targets were installed at the test site or on the test building, the image correlation relies on either the manual selection of point features or the automatic detection of blob features of the background scene (i.e., ground level).

At the beginning of this the step, the LiDAR point cloud data are used to generate an orthorectified reference image (or orthoimage) [Fig. 4(a)]. While the point cloud data are geometrically accurate, the point color texture is much less reliable and the point density varies substantially over the scene. Because the LiDAR orthoimage does not appear photorealistic, this prevents automatic feature detection and correspondence with the video frames. To this end, point correspondences are established manually in the LiDAR point cloud and the reference frame (Fig. 4). These manually selected point correspondences allow for estimation of a homography matrix (Hartley and Zisserman 2003), which maps the pixel coordinates in the undistorted reference frame to the geometrically accurate points in the LiDAR orthoimage. While a minimum of four-point correspondences are needed to estimate the homography, approximately 20 spatially distributed points at the ground level were used to reduce errors associated with the manual correspondence selection. The homography matrix (projective transformation) estimated using these point correspondences is then applied to the reference frame to remove the ground-level perspective distortion (warping). However, it is noted that the perspective correction at the ground level does not completely remove the distortion at the roof level, because the effects of perspective distortion vary for different depths of field.

Following the manual correction of the reference frame using the georeferenced LiDAR orthoimage, region-based pixel features are identified at the ground level in the reference and all subsequent frames using the speed-up robust features (SURF) algorithm (Bay et al. 2008). Because the variation of camera views and color features among different frames within an individual test video are much smaller than those between a video frame and the LiDAR orthoimage, the feature correspondences between the video frames can be identified automatically without the need for manual feature selection. During this automatic feature detection step, the region of the frames containing the building is excluded due to its movement. Once SURF features are identified in all video frames, the features in the subsequent frames are compared to those in the reference frame in order to find correspondences. For every feature in each subsequent frame, the feature matching algorithm calculates the sum of squared differences between the feature vectors in the reference frame and the subsequent frame. It is noted that approximately 3,000–7,000 features were typically identified in the video frames, and approximately 300–500 correspondences were ultimately identified between each subsequent frame and the reference frame. The resulting correspondences between the subsequent frames

and the reference frame allow for the estimation of a homography matrix (or projective transformation) that maps the pixels of the subsequent frames to the orthorectified reference video frame. At the conclusion of this step, all the video frames are stabilized with respect to the ground, allowing only the motion of the building roof to be extracted in the remaining procedures.

Roof Feature Detection and Displacement Extraction

Correction of the video frames by removing the perspective distortion and UAV drift effects produces a sequence of orthorectified images stabilized at the ground level. To obtain the building displacements at the roof level, Step 3 analyzes the orthoimage sequence using a two-step method: (1) edge-based detection of roof features, and (2) displacement extraction via established frame-to-frame correspondence of the detected feature points. Given the lack of textured features and the rectangular tiling pattern at the roof level, the roof displacements are estimated by tracking the location and orientation of the linear (line) features as detected via the Canny edge detection algorithm (Canny 1986). Selection of the proper features may depend on the perceived texture characteristics of the image frames (e.g., building surface materials, geometry, and illumination conditions). Highly textured building surfaces with sufficient feature density, for instance, may warrant alternative feature tracking and matching algorithms such as the Lucas-Kanade optical flow method (Lucas and Kanade 1981). Nonetheless, herein, the target features of the building roof are selected as two straight lines in the longitudinal direction (L1 and L2) and one in the transverse direction (T1), which are subsequently used to determine the two intersections (P1 and P2) [Fig. 5(a)]. In this analysis procedure, the linear features are successively detected using three predefined rectangular regions of interest (ROIs) located in the vicinity of individual target features. In each ROI, the Canny edge detection algorithm identifies the discrete two-sided edge point pairs [dots shown in Fig. 5(b)] to allow for linear regression of the target line [line shown in Fig. 5(b)] within the pixel coordinates. The regressed lines are then used to solve for the pixel coordinates of the two intersections. Although the edge points detected from different video frames may differ due to the variations of illumination condition and camera pose [Fig. 5(b)], the number of detected edge points is sufficiently large (typically 600–1,000 points) to ensure the robustness and accuracy of the linear regression.

Tracking the roof displacements at different time instances relies on the variations of intersection points P1 and P2 in the subsequent frames relative to those in the reference frame. As shown in Fig. 6, displacement tracking requires that the following two types of geometric transformations be estimated: (1) world coordinate system versus pixel coordinate system, and (2) reference frame versus subsequent frame (in world coordinate system). The transformation between the two coordinate systems represents a similarity transformation that involves the effects of scale, rotation, and translation. It is estimated by correlating the pixel coordinates of the tracked features (i.e., P1 and P2) in the reference orthoimage with their world coordinates. For instance, Fig. 6(a) shows the known dimensions of the square region (marked with the dashed lines) with an equal edge length of 122 cm (determined using LiDAR data) allowed the world coordinates of the intersections be determined. The estimated transformation between the two coordinate systems is then used to transform the intersections in all video frames from the pixel coordinates into the world coordinates. Importantly, this transformation defines a scale factor between the world coordinate system and pixel coordinate system. Because the distance between the two intersections had a real length of 122 cm in world coordinates and about 160 pixels in pixel coordinates, the scale factor is determined as 0.76 cm/pixel [Fig. 6(a)]. This scale factor is useful for comparing the relative resolution of the video frames taken during different earthquake tests.

With the assumption that the roof moves rigidly in-plane during the earthquake tests, a rigid transformation is estimated using correspondences of the world coordinates of the tracked features [Fig. 6(b)]. In the final step of the roof feature tracking, the roof displacements (i.e., two translations and one rotation) are extracted by decomposing the rigid transformation matrix between the reference and subsequent frames.

Filtering of Video-Based Results

As discussed in the earlier section, the perspective correction used to stabilize the ground level does not effectively remove the UAV drift-induced distortion of the roof level because it corresponds to a

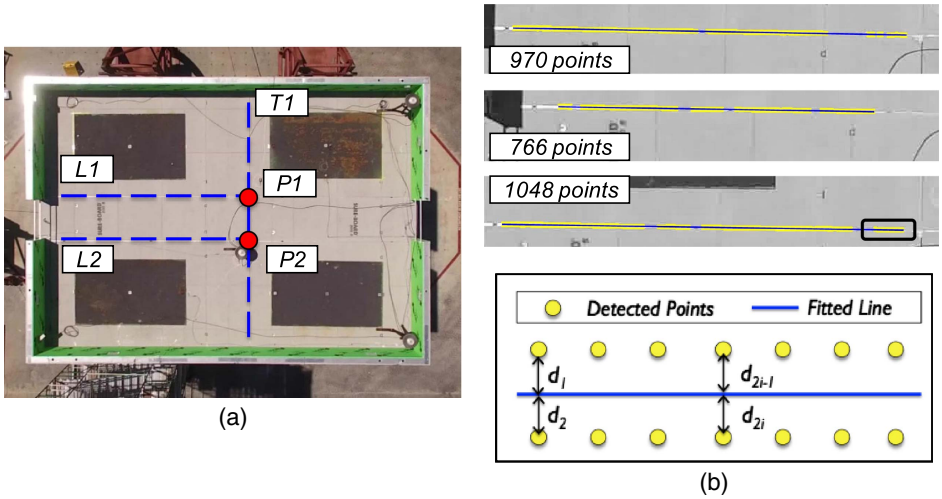

Fig. 5. Roof feature detection and line regression adopted in the validation study: (a) target linear features and intersection points; and (b) detected edge points from three different video frames.

J. Comput. Civ. Eng., 2020, 34(6): 04020045

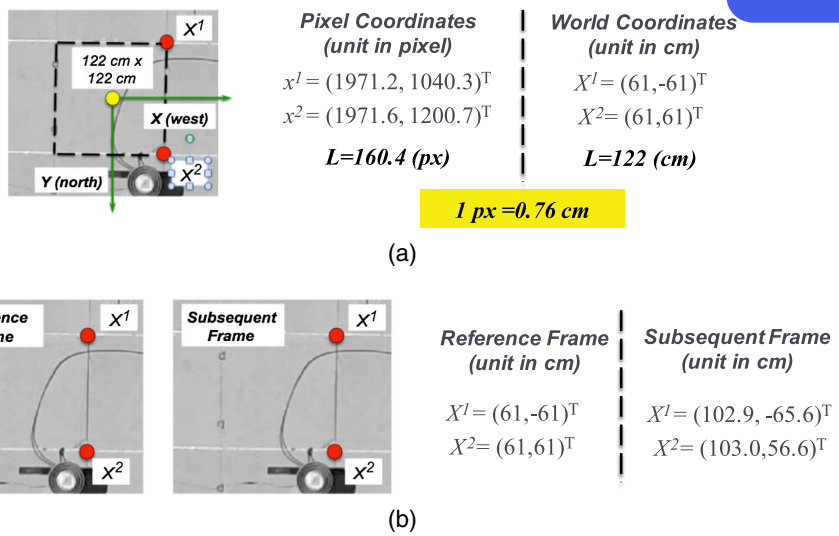

Fig. 6. Geometric transformation of roof feature points for representative ROI: (a) world coordinates versus pixel coordinates associated with a single frame; and (b) reference frame and subsequent frame (in world coordinate system).

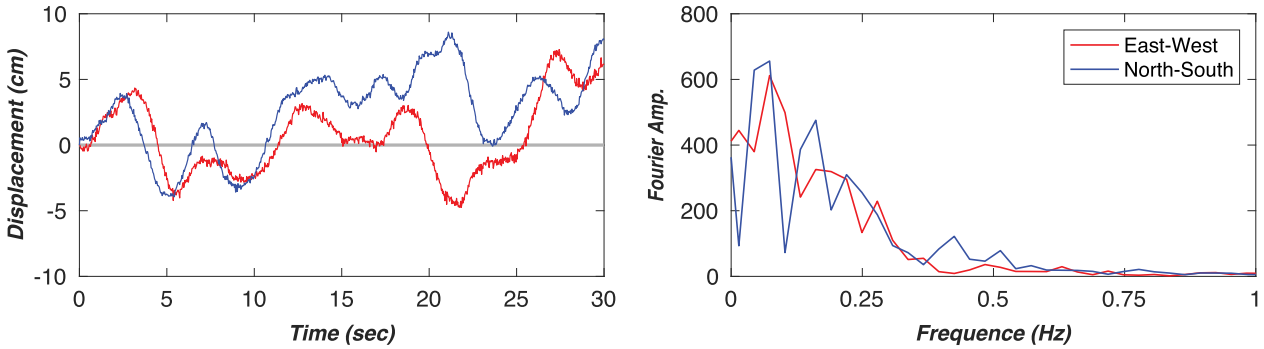

Fig. 7. Roof displacements of intersection point P1 extracted from the preevent of Test EQ7 and the associated Fourier amplitude spectra (horizontal gray lines in time histories indicate the zero-displacement baseline).

scene depth different from that of the ground level. To demonstrate the effect of UAV drift-induced roof distortion, Fig. 7 shows the video-based displacement results of the roof intersection point P1 [Fig. 5(a)] extracted from the preevent of Test EQ7 (a 30-s segment prior to the onset of earthquake shaking) and the associated Fourier amplitude spectra. Because the building was essentially stationary during the preevent stage, the unfiltered (raw) roof displacements extracted from the video analysis represent the error metrics of the UAV drift-induced roof-distortion effect. These preevent video analysis results indicate that the UAV drift-induced roof distortion produces a peak displacement error of ~10 cm in both the east-west and north-south directions In addition, the Fourier amplitude spectra reveal that these drift-induced roof displacements in both horizontal directions are characterized by frequency contents primarily in the low-frequency range (0–0.5 Hz).

In this regard, the pre- or postevent displacement tracking results are investigated to provide guidance on the implementation of a high-pass filtering strategy for correcting the effect of UAV drift-induced distortion at the roof level. The filter adopted in this exercise is a tenth-order Butterworth high-pass filter, although other filter types may also be considered for the same purpose. The high-pass corner frequency is determined such that the filtered pre- or postevent displacement tracking results are acceptably small (e.g., <1 cm). Fig. 8 presents the variation of the root-mean-square (RMS) roof displacements (intersection point P1) during the preevent of Test EQ7 with respect to the corner frequency (within the 0.05–0.5 Hz interval). This sensitivity study indicates that the displacement errors (in both horizontal directions) drop substantially with the increase of corner frequency until it reaches approximately 0.25 Hz. Although further increase of the corner frequency continues to reduce the displacement errors, these errors are much less sensitive to the corner frequency change. Because the preevent roof-displacement errors filtered using the high-pass corner frequency of 0.25 Hz are sufficiently small (~0.5 cm), this value is selected for correcting the roof-displacement responses during the earthquake shaking of Test EQ7. It is also noted that because the fundamental natural frequency of the building ranged between 2 and 4 Hz (depending on the severity of structural damage) during the earthquake test program (Wang and Hutchinson 2020), a high-pass corner frequency of 0.25 Hz is sufficiently low for preserving the real building responses.

To demonstrate the effect of high-pass corner frequency on the roof-displacement tracking results, Fig. 9 compares the absolute roof longitudinal (east-west) displacement responses during Test EQ7. The roof-displacement responses obtained from the motion-tracking method, including both the preevent results and those

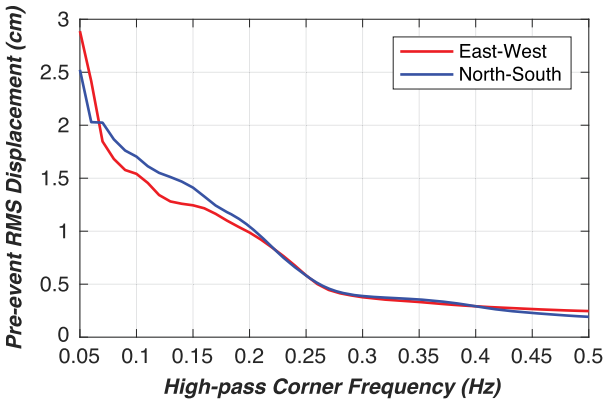

Fig. 8. Sensitivity of the RMS roof displacements with respect to the corner frequency during the preevent of Test EQ7.

during the earthquake shaking, are filtered using three strategically selected high-pass corner frequencies: 0.1, 0.25, and 0.5 Hz. Whereas 0.1 and 0.5 Hz may represent the lower and upper bound values of the corner frequency range according to the frequency characteristics obtained from the preevent results analysis (Fig. 7), 0.25 Hz is an optimized value as determined from the preevent result analysis. Fig. 9(a) reveals that the preevent displacement response of the intersection point P1 is reasonably small when filtered by the two larger corner frequencies (0.25 and 0.5 Hz), whereas the lower bound corner frequency (0.1 Hz) does not appear effective for correcting the UAV drift-induced roof distortion as manifest by the presence of substantial displacement response during the preevent stage. This is attributed to the fact that the UAV drift-induced displacements at the roof level encompass frequency contents substantially larger than 0.1 Hz (Fig. 7). As shown in Fig. 9(b), the baseline drift as evident in the unfiltered roof-displacement response at the beginning of the earthquake shaking remains apparent when the displacement is filtered using the lower bound corner frequency (0.1 Hz). It is also important to note that although the upper bound corner frequency of 0.5 Hz appears effective for correcting the preevent roof displacements, the use of this corner frequency on the earthquake shaking response leads to significant reduction of the roof displacement compared to the GPS measurements, whereas the same response filtered with the optimized corner frequency (0.25 Hz) correlates well with the GPS measurements. This is due to the fact that using the frequency of 0.5 Hz may modify the roof-displacement response contributed by the input earthquake motion, because the absolute roof displacement consists of the contribution of the input earthquake motion (shake table movement) and the roof displacement relative to the shake table (which is dominated by the natural vibration frequency of the building).

As such, selecting an appropriate high-pass corner frequency for UAV drift-induced roof-distortion correction needs to address the following two considerations: (1) the preevent roof displacement filtered using the selected corner frequency needs to be sufficiently small (e.g., RMS response <1 cm), and (2) the selected corner frequency needs to remain sufficiently small to prevent modifying the real building responses, particularly those contributed by the earthquake input motion. It is noted, however, that this high-pass filtering strategy may not be effective for capturing any residual (permanent) roof displacements achieved at the end of the earthquake tests.

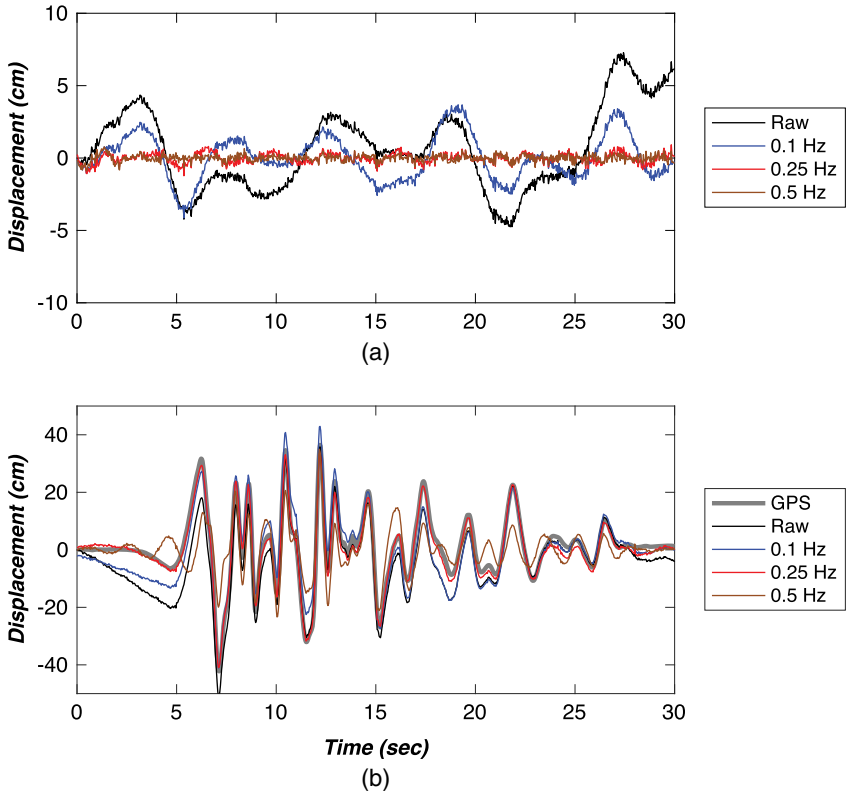

Fig. 9. Effect of high-pass corner frequency on the roof-displacement results during test EQ7: (a) preevent response; and (b) response during the earthquake shaking.

J. Comput. Civ. Eng., 2020, 34(6): 04020045

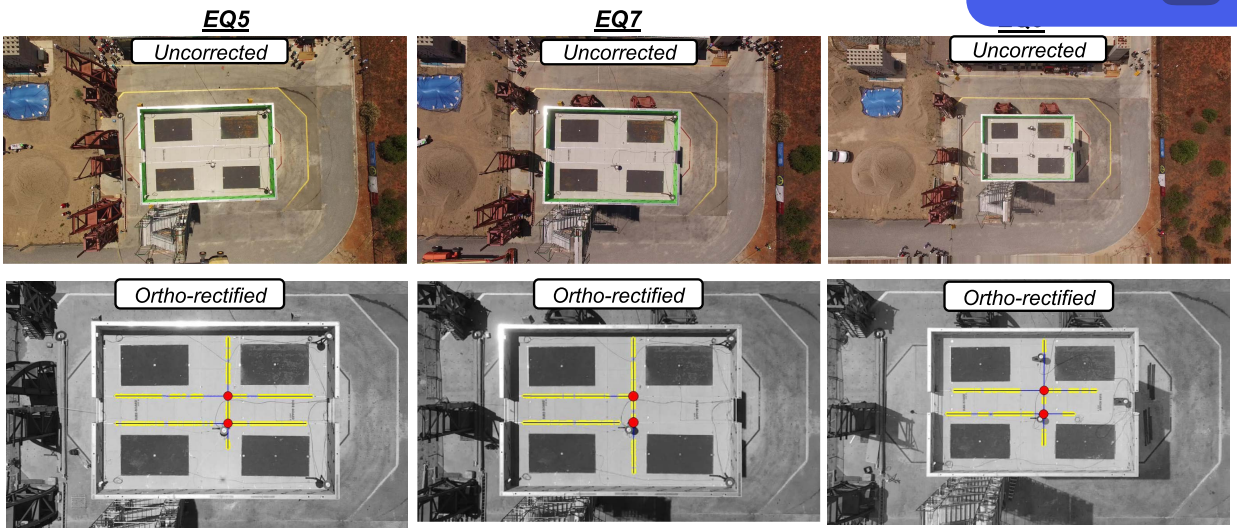

Fig. 10. Uncorrected and orthorectified reference image frames for the three test videos (note that the detected roof features are overlaid with the orthorectified reference images).

Results and Discussion

Validation of Motion-Tracking Results

To evaluate the effectiveness of the proposed UAV-based video methodology, the roof displacements of the test building are analyzed using the top-view test videos collected during three earthquake tests with different motion intensities, namely, EQ5 (50% scale design event), EQ7 (150% scale design event), and EQ9 (150% scale design event). Although the test videos were intended to monitor the structural response from a consistent viewpoint, the position of the on-board camera varied during individual tests. For instance, the estimated camera location was 40–45 m above the ground during Tests EQ5 and EQ7 but exceeded 60 m during Test EQ9. Fig. 10 shows the uncorrected (original) and the orthorectified reference frames for the three test videos. The uncorrected reference frames clearly indicate that the dimension and orientation of the ground level shown in the reference frame differ among the three test videos as a result of the variation of the camera viewpoints. In contrast, the ground level as shown in the different orthorectified frames is well aligned following the perspective correction using the LiDAR orthoimage as the reference. Despite the consistency of the ground level among different test videos, the roof projection in the orthorectified frame of test video EQ9 is substantially smaller than its size in the other two frames (EQ5 and EQ7). This difference is due to the larger camera-to-roof distance and the ground-level projective transformation applied over the entire image frames.

Fig. 11 compares the absolute roof longitudinal (east-west) displacement histories obtained from the video analysis overlaid with the GPS measurements during the three select earthquake tests (EQ5, EQ7, and EQ9) and the associated error responses (i.e., the discrepancies between the video analysis results and the GPS measurements). The transverse (north-south) displacements of the roof are not presented in the figure due to the small amplitude (<2 cm) of these responses. The high-pass filtering strategy previously presented is adopted to correct the video-based roof displacements extracted from Tests EQ5 and EQ7. Based on the pre- or postevent displacements analysis and the selection criteria as mentioned in the previous section, the high-pass corner frequency is chosen as 0.3 Hz for Test EQ5 and 0.25 Hz for Test EQ7. It is noted that the roof displacement extracted from Test EQ9 does not involve high-pass filtering, because such a strategy would remove the residual roof displacement achieved at the end of the earthquake test and consequently modify the baseline of the dynamic displacement response. These comparisons indicate that the roof displacements from the UAV-based video analysis are in good agreement with the GPS measurements. The RMS error (the discrepancy between the video-based results and GPS measurements) ranges between 1 and 2 cm for Tests EQ5 and EQ7 and is only slightly larger (2.5 cm) for Test EQ9, because high-pass filtering is not employed to correct the video analysis results in consideration of preserving the residual displacement at the end of Test EQ9.

Table 2 compares the peak and residual roof displacements obtained from the video analysis with the GPS measurements. With the application of a high-pass filter to the video-based results, the absolute errors of the peak displacements remain reasonably small (only 2 cm as the maximum value) for both Tests EQ5 and EQ7. Due to the small amplitude of the peak roof displacements during Test EQ5 (~10 cm), the relative error, which is taken as the percentage of the absolute error divided by the absolute peak response, is approximately 15% for Test EQ5, which is notably larger than those of Test EQ7 (~5%). The absolute errors reach as much as 6 cm for Test EQ9, because the results involve the UAV drift-induced distortion at the roof level in the absence of high-pass filtering. In addition, the video analysis results during Test EQ9 (final earthquake test) allow for evaluation of the static residual displacement of the building roof at the end of the test program, which is determined by averaging the video-based displacement response at the end of the earthquake test using a 2-s window (between 23 and 25 s). The video analysis results provide a reasonable estimate of this static residual displacement (differing from GPS results by only ~1 cm). Comparison of the video analysis results against the GPS measurements demonstrates that the proposed UAV-based video analysis provides an effective means for tracking the dynamic roof-displacement responses and the static residuals during these earthquake tests.

Limitations of the Proposed Methodology

Validation of the motion-tracking results using the full-scale building shake table experiments demonstrates the potential for using

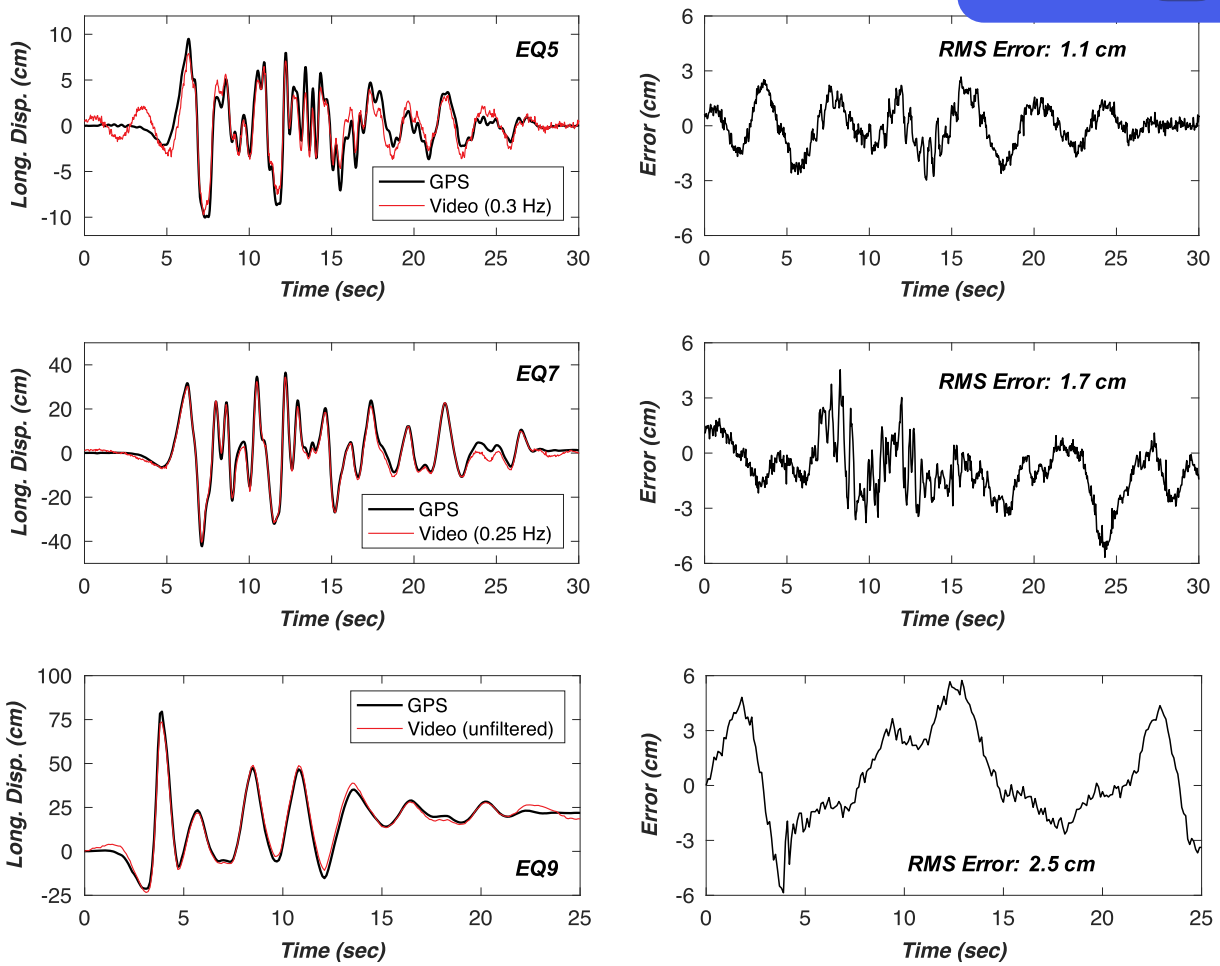

Fig. 11. Comparison of the UAV video-based absolute roof longitudinal displacements with the GPS measurements and the associated response errors during the three earthquake tests.

Table 2. Comparison of peak and residual roof displacements obtained from the video analysis with the GPS measurements

		Peak roof displacement (positive)			Peak roof displacement (negative)			Residual roof displacement		
Test name	Motion intensity	UAV (cm)	GPS (cm)	Error (cm)	UAV (cm)	GPS (cm)	Error (cm)	UAV (cm)	GPS (cm)	Error (cm)
EQ5	50% design	8.1	9.5	1.4 (14.7%)	9.7	10.0	0.3 (3.1%)	N/A	N/A	N/A
EQ7	150% design	34.4	36.5	2.1 (5.6%)	40.4	42.2	1.8 (4.4%)	N/A	N/A	N/A
EQ9	150% design	73.7	79.5	5.8 (7.3%)	23.4	21.3	2.1 (10.0%)	20.9	22.0	1.1 (7.1%)

Note: GPS = global positioning system; UAV = unmanned aerial vehicle (video); number in the parentheses represents the relative error (= percentage of the absolute error divided by the absolute peak response).

commercial UAV platforms to monitor dynamic structural responses. The proposed methodology is particularly useful when accurate estimation of camera pose is difficult, for example, due to the constraints discussed earlier. However, important limitations exist with regard to the implemented UAV motion-tracking procedures in practice. Among them, perhaps the most prominent include the following: (1) the camera frame rate (30 Hz) may be insufficient for capturing the response of structures with dominant high-frequency modes (15 Hz or larger), (2) the use of a high-pass filtering strategy for correcting UAV drift-induced distortion effects may pose challenges for monitoring flexible structures, in particular those with their dominant frequencies smaller than or comparable to the high-pass corner frequency (e.g., tall buildings and long-span bridges), and (3) very low-amplitude structural responses (e.g., subcentimeter-level displacements) cannot be identified given the level of accuracy as demonstrated in the validation studies. Whereas the capability for capturing high-frequency responses can be enhanced by using cameras with higher frame rates, extending the effectiveness of the proposed methodology for monitoring low-frequency and low-amplitude structural responses requires significant accuracy in the estimation of the camera pose. Improvement of the camera pose estimation may be achieved with the support of auxiliary data collected by on-board navigation sensing systems (e.g., inertial sensors, range or depth sensors) and/or the placement of georeferenced targets on the camera background scene (e.g., Yoon et al. 2018).

It is also noted that the ground features (or reference objects) are subjected to earthquake displacements rather than remaining stationary during a real earthquake. Under such a scenario, stabilizing the video frames at the ground level would conceptually allow for capturing the building roof-displacement responses relative to the ground instead of the absolute displacement of the building. Nonetheless, stabilizing the video frames with a set of moving ground features has not been attempted and would require additional validation studies to confirm the effectiveness of the proposed motion-tracking method for its applications in real earthquakes.

Computational Performance

The proposed methodology is implemented as an off-line process, because the analysis procedures involve the following two manual steps: (1) orthorectifying the reference (first) video frame against a LiDAR orthoimage by manual selection of the ground-level features (Step 2a of Fig. 3), and (2) determining a high-pass corner frequency using the pre- or postevent video analysis results for correcting the UAV drift-induced distortion effects during the earthquake shaking. The remaining steps are all associated with automatic frame-by-frame image processing: (1) identifying SURF features at the ground level and establish the feature correspondences (Step 2b of Fig. 3), and (2) extracting the linear edge features at the building roof and line fitting (Step 3 of Fig. 3). The video frames are all processed using a laptop computer with a 2.7-Hz Intel Core i5 processor and 8 Gb memory. The average processing time for each video frame is approximately 2,170 ms, namely, 350 ms for ground SURF feature matching and 1,820 ms for roof edge feature detection and line fitting.

Conclusions

UAV imagery has recently emerged as an effective structural health monitoring tool for operational condition inspection and post-disaster damage assessment of civil structures (e.g., bridges and buildings). However, the use of such sensing techniques for quantitatively tracking the subtle (centimeter-level) variations of structural dynamic responses has been limited, largely due to the difficulties related to obtaining accurate location measurements for the majority of small UAV platforms. To fill this research gap, a UAV-based video analysis methodology is developed for tracking the roof-displacement responses of a full-scale six-story CFS building using the top-view test videos collected during a series of shake table tests at various earthquake intensities. The proposed methodology first corrects the UAV drift-induced image perspective distortion and misalignment and subsequently extracts the dynamic displacements of the building by establishing frame-to-frame correspondences of the identified image features. In addition, the motion-tracking errors are investigated by analyzing the frequency content of the displacement responses extracted from the pre- or postevent videos. Investigating the error characteristics of video-based results while the building remains stationary provides useful guidance for further correction of the building responses during dynamic earthquake shaking. Validation of the UAV-based video analysis results against the GPS measurements demonstrates the effectiveness of the proposed methodology for quantifying the dynamic displacement responses of full-scale buildings during low- to high-intensity earthquake shaking. Without relying on the accurate position of the UAV on-board cameras, the video analysis results achieve a level of precision (less than 2 cm RMS errors when the high-pass filtering strategy is used) that is considered acceptable for engineering applications.

Because the UAV-based motion-tracking results are validated using only a limited set of test videos taken from the top view, admittedly, additional studies are needed to confirm the robustness and reliability of the proposed methodology, particularly considering alternative camera views (e.g., elevation views and oblique views) or test structures of different scales. Moreover, improved accuracy of the UAV-based motion-tracking results is needed to extend its applicability of monitoring low-frequency and low-amplitude structural responses. Future studies may attempt fusing the UAV imagery data with auxiliary data collected by other on-board sensing systems (e.g., inertial navigation sensors, depth or range sensors) in an effort to continually improve camera pose estimation and ultimately enhance the performance of tracking dynamic structural responses.

Data Availability Statement

Some or all data, models, or code that support the findings of this study are available from the corresponding author upon request. These items include (1) measured building roof GPS displacement responses, and (2) UAV video footage.

Acknowledgments

The UAV video-based analysis study was partially supported by the National Institute of Standards and Technology (NIST) (Award No. 70NANB17H211). The CFS building shake table test project used to validate the proposed methodology was supported through a collaboration between two academic institutions (University of California, San Diego and Worcester Polytechnic Institute), two government or institutional granting agencies (Department of Housing and Urban Development and the California Seismic Safety Commission), and 15 industry partners [among the larger collaborations were the California Expanded Metal Products Co. (CEMCO), Sure-Board, DCI Engineers, and SWS Panel]. The Jacobs School of Engineering and Department of Structural Engineering at UCSD also provided matching support for the experimental program. The participation of Scripps Institution of Oceanography at UCSD was funded by NASA Grant No. NNX16AM04A. The aforementioned support is greatly appreciated. Finally, we acknowledge the students and staff of the UCSD outdoor shake table test facility for their support during the building test program that was utilized for validation herein.

References

Abdel-Qader, I., O. Abudayyeh, and M. E. Kelly. 2003. "Analysis of edge-detection techniques for crack identification in bridges." *J. Comput. Civ. Eng.* 17 (4): 255–263. https://doi.org/10.1061/(ASCE)0887-3801(2003)17:4(255).

AISI (American Iron and Steel Institute). 2007. *North American standard for cold-formed steel farming—Lateral design*. AISI S213. Washington, DC: AISI.

AISI (American Iron and Steel Institute). 2012. *North American specification for the design of cold-formed steel structural members*. AISI S100. Washington, DC: AISI.

ASCE. 2010. *Minimum design loads for buildings and other structures*. ASCE 7. Reston, VA: ASCE.

Bay, H., A. Ess, T. Tuytelaars, and L. Van Gool. 2008. "Speeded-up robust features (SURF)." *Comput. Vision Image Understanding* 110 (3): 346–359. https://doi.org/10.1016/j.cviu.2007.09.014.

Bouguet, J. Y. 2015. "Camera calibration toolbox for MATLAB." Accessed October 12, 2017. http://vision.caltech.edu/bouguetj/calib_doc.

Canny J. 1986. "A computational approach to edge detection." *IEEE Trans. Pattern Anal. Mach. Intell.* 8(6), 679–698.

Dominici, D., M. Alicandro, and V. Massimi. 2017. "UAV photogrammetry in the post-earthquake scenario: Case studies in L'Aquila" *Geomatics Nat. Hazards Risk* 8 (1): 87–103. https://doi.org/10.1080/19475705.2016.1176605.

Ellenberg, A., A. Kontsos, F. Moon, and I. Bartoli. 2016. "Bridge related damage quantification using unmanned aerial vehicle imagery." *Struct. Control Health Monit.* 23 (9): 1168–1179. https://doi.org/10.1002/stc.1831.

Franke, K. W., K. M. Rollins, C. Ledezma, J. D. Hedengren, D. Wolfe, S. Ruggles, B. Christopher, and B. Reimschiissel. 2016. "Reconnaissance of two liquefaction sites using small unmanned aerial vehicles and structure from motion computer vision following the April 1, 2014 Chile earthquake." *J. Geotech. Geoenviron. Eng.* 143 (5): 04016125. https://doi.org/10.1061/(ASCE)GT.1943-5606.0001647.

Fukuda, Y., M. Q. Feng, and M. Shinozuka. 2010. "Cost-effective vision-based system for monitoring dynamic response of civil engineering structures." *Struct. Control Health Monit.* 17 (8): 918–936. https://doi.org/10.1002/stc.360.

Gao, X. S., X. R. Hou, J. Tang, and H. F. Cheng. 2003. "Complete solution classification for the perspective-three-point problem." *IEEE Trans. Pattern Anal. Mach. Intell.* 25 (8): 930–943. https://doi.org/10.1109/TPAMI.2003.1217599.

Gao, Y., and K. M. Mosalam. 2018. "Deep transfer learning for image-based structural damage recognition." *Comput.-Aided Civ. Infrastruct. Eng.* 33 (9): 748–768. https://doi.org/10.1111/mice.12363.

Hartley, R., and A. Zisserman. 2003. *Multiple view geometry in computer vision*. Cambridge, UK: Cambridge University Press.

Hutchinson, T. C., and Z. Chen. 2006. "Improved image analysis for evaluating concrete damage." *J. Comput. Civ. Eng.* 20 (3): 210–216. https://doi.org/10.1061/(ASCE)0887-3801(2006)20:3(210).

Hutchinson, T. C., and F. Kuester. 2004. "Monitoring global earthquake-induced demands using vision-based sensors." *IEEE Trans. Instrum. Meas.* 53 (1): 31–36. https://doi.org/10.1109/TIM.2003.821481.

Hutchinson, T. C., X. Wang, G. Hegemier, B. Meacham, and P. Kamath. 2018. "Earthquake and post-earthquake fire testing of a mid-rise cold-formed steel framed building." In *Proc., 11th National Conf. on Earthquake Engineering*. Los Angeles: Earthquake Engineering Research Institute.

Koch, C., G. M. Jog, and I. Brilakis. 2012. "Automated pothole distress assessment using asphalt pavement video data." *J. Comput. Civ. Eng.* 27 (4): 370–378. https://doi.org/10.1061/(ASCE)CP.1943-5487.0000232.

Lee, J. J., and M. Shinozuka. 2006. "A vision-based system for remote sensing of bridge displacement." *NDT and E Int.* 39 (5): 425–431. https://doi.org/10.1016/j.ndteint.2005.12.003.

Lepetit, V., F. Moreno-Noguer, and P. Fua. 2009. "EPnP: An accurate O(n) solution to the PnP problem." *Int. J. Comput. Vision* 81 (2): 155–166. https://doi.org/10.1007/s11263-008-0152-6.

Lucas, B. D., and T. Kanade. 1981. "An iterative image registration technique with an application to stereo vision." In *Proc., 7th Int. Joint Conf. on Artificial Intelligence*, 674–679. Pasadena, CA: International Joint Conferences on Artificial Intelligence Organization.

Meyer, D., M. Hess, E. Lo, C. E. Wittich, T. C. Hutchinson, and F. Kuester. 2015. "UAV-based post disaster assessment of cultural heritage sites following the 2014 South Napa Earthquake." In vol. 2 of *Proc., 2015 Digital Heritage*, 421–424. New York: IEEE.

Morgenthal, G., and N. Hallermann. 2014. "Quality assessment of unmanned aerial vehicle (UAV) based visual inspection of structures." *Adv. Struct. Eng.* 17 (3): 289–302. https://doi.org/10.1260/1369-4332.17.3.289.

Reagan, D., A. Sabato, and C. Niezrecki. 2018. "Feasibility of using digital image correlation for unmanned aerial vehicle structural health monitoring of bridges." *Struct. Health Monit.* 17 (5): 1056–1072. https://doi.org/10.1177/1475921717735326.

Schonberger, J. L., and J. M. Frahm. 2016. "Structure-from-motion revisited." In *Proc., IEEE Conf. on Computer Vision and Pattern Recognition*, 4104–4113. New York: IEEE.

Torok, M. M., M. Golparvar-Fard, and K. B. Kochersberger. 2013. "Image-based automated 3D crack detection for post-disaster building assessment." *J. Comput. Civ. Eng.* 28 (5): A4014004. https://doi.org/10.1061/%28ASCE%29CP.1943-5487.0000334.

Wahbeh, A. M., J. P. Caffrey, and S. F. Masri. 2003. "A vision-based approach for the direct measurement of displacements in vibrating systems." *Smart Mater. Struct.* 12 (5): 785. https://doi.org/10.1088/0964-1726/12/5/016.

Wang, X., and T. C. Hutchinson. 2020. "Evolution of modal characteristics of a mid-rise cold-formed steel building during construction and earthquake testing." *Earthquake Eng. Struct. Dyn.* https://doi.org/10.1002/eqe.3316.

Wang, X., T. C. Hutchinson, G. Hegemeir, S. Gunisetty, P. Kamath, and B. Meacham. 2016. *Earthquake and post-earthquake fire performance of a mid-rise cold-formed steel framed building—Test program and test results: Rapid Release Report*. Rep. No. SSRP-16/07. La Jolla, CA: Univ. of California, San Diego.

Wang, X., T. C. Hutchinson, G. Hegemeir, S. Gunisetty, P. Kamath, and B. Meacham. 2018. *Earthquake and post-earthquake fire performance of a mid-rise cold-formed steel framed building—Test program and test results: Final report*. Rep. No. SSRP-16/08. La Jolla, CA: Univ. of California, San Diego.

Westoby, M. J., J. Brasington, N. F. Glasser, M. J. Hambrey, and J. M. Reynolds. 2012. "'Structure-from-motion' photogrammetry: A low-cost, effective tool for geoscience applications." *Geomorphology* 179 (Dec): 300–314. https://doi.org/10.1016/j.geomorph.2012.08.021.

Wood, R. L., D. T. Gillins, M. E. Mohammadi, F. Javadnejad, H. Tahami, M. N. Gillins, and Y. Liao. 2017. "2015 Gorkha post-earthquake reconnaissance of a historic village with micro unmanned aerial systems." In *Proc., 16th World Conf. on Earthquake Engineering*. Tokyo: International Association for Earthquake Engineering.

Yeum, C. M., and S. J. Dyke. 2015. "Vision-based automated crack detection for bridge inspection." *Comput.-Aided Civ. Infrastruct. Eng.* 30 (10): 759–770. https://doi.org/10.1111/mice.12141.

Yoon, H., H. Elanwar, H. Choi, M. Golparvar-Fard, and B. F. Spencer. 2016. "Target-free approach for vision-based structural system identification using consumer-grade cameras." *Struct. Control Health Monit.* 23 (12): 1405–1416. https://doi.org/10.1002/stc.1850.

Yoon, H., V. Hoskere, J. W. Park, and B. F. Spencer. 2017. "Cross-correlation-based structural system identification using unmanned aerial vehicles." *Sensors* 17 (9): 2075. https://doi.org/10.3390/s17092075.

Yoon, H., J. Shin, and B. F. Spencer. 2018. "Structural displacement measurement using an unmanned aerial system." *Comput.-Aided Civ. Infrastruct. Eng.* 33 (3): 183–192. https://doi.org/10.1111/mice.12338.